Solar Energy Materials and Solar Cells 172 (2017) 99–107

Contents lists available at ScienceDirect

Solar Energy Materials and Solar Cells

journal homepage: www.elsevier.com/locate/solmat

Study on solidification process of sodium acetate trihydrate for seasonal solar thermal energy storage

Zhiwei Ma, Huashan Bao*, Anthony Paul Roskilly

Sir Joseph Swan Centre for Energy Research, Newcastle University, Newcastle upon Tyne NE1 7RU, UK

ARTICLE INFO

Keywords:
Sodium acetate trihydrate
Solidification process
Thermo-physical properties
Modelling
Energy density

ABSTRACT

The phase change of sodium acetate (SA) aqueous solution to sodium acetate trihydrate (SAT) requires large supercooling degree, then the aqueous solution can be at liquid state at fairly low temperature without releasing the stored latent heat. Such a feature makes SAT a promising material for seasonal solar thermal energy storage. The present study firstly summarized the thermo-physical properties of the solid SAT and liquid SA aqueous solution at different temperatures and concentrations, including equilibrium temperatures, densities, specific heats and thermal conductivities. The calculation methods of these properties have been established. Secondly, with the aid of the above properties, a mathematic model of the thermal discharge process of the storage system, i.e. the solidification process of supercooled SA aqueous solution, was built based on the heat transfer between the phase changing material within a single storage tube and the external flowing heat transfer fluid (HTF). The experimentally obtained SAT crystal growth rate and the enthalpy change of solidifying supercooled SA aqueous solution were employed to aid the modelling. The discharge temperature and thermal power of the storage system were numerically obtained and analysed. The influence of the ambient temperature, the mass flow rate as well as the heat transfer coefficient of the HTF on the thermal discharge performance were discussed. Finally, the seasonal thermal storage density of SAT was given and compared to that of water and some sorption materials.

1. Introduction

Space heating and domestic hot water consumes the majority energy demanded by residential buildings, e.g. about 82% in Europe [1]. On the other side, the amount of solar radiation projected to a typical house roof normally exceeds the total amount of heat needed for the house heating over a year. That implies that the seasonal solar thermal energy storage seems to be the most feasible way to achieve completely 'free' house heating. The well-known three types of thermal energy storage technologies, i.e. sensible heat storage, latent heat storage and chemical reaction heat storage, are all available for seasonal solar thermal energy storage [1–3].

The latent heat storage by phase change material (PCM) provides larger thermal energy storage density than that of sensible heat storage; although its storage density is not competitive to chemical reaction storage, the system is simpler, more robust and reliable than chemical reaction system. Salt hydrate as PCM distinctively features large supercooling degree, which is regarded as one of the drawbacks that impedes latent heat releasing at desirable temperature level. However, this drawback can be treated as a valuable merit for a different purpose – the long-term thermal energy storage; because of the large supercooling degree, the melted salt hydrate can remain at liquid state at relatively low temperature without losing any stored latent heat, only sensible heat is lost throughout the storage period, therefore the system is not necessarily thermal insulated but can still discharge the majority of the stored thermal energy.

Sodium acetate trihydrate (SAT) is one of the typical salt hydrate PCMs, which has the melting temperature of 58.0 °C and latent heat of 264.0 kJ/kg [4]. These properties and the low cost make it a suitable PCM for residential heating. Furthermore, the melted SAT can be easily supercooled to below 0 °C with a supercooling degree as large as 80 °C [5], so that the latent heat can be preserved during long-term storage. Recently, Dannemand et al. have reported a series of study on using SAT for seasonal solar thermal energy storage [6–9]. The authors simulated the storage system using TRNSYS and concluded that the seasonal solar thermal energy storage with 7 PCM modules of 150 L each can satisfy 80% of annual space heating and hot water of a house in Danish climate [6]. The solidification behavior of SAT with thickening agent, including carboxymethyl cellulose (CMC) and xanthan rubber, and the thermal conductivity enhancement by adding graphite powder were experimentally tested and discussed in the work [7], where liquid CO_2 was used to initiate the crystallization of supercooled

* Corresponding author.
E-mail address: huashan.bao@newcastle.ac.uk (H. Bao).

http://dx.doi.org/10.1016/j.solmat.2017.07.024
Received 12 January 2017; Received in revised form 3 May 2017; Accepted 18 July 2017

Nomenclature

A,B,C,D,E,F,G	equation constant (-)
c	molar density (mol/dm^3)
c_p	specific heat (J/(kg K))
D	diameter (m)
D_e	hydraulic diameter (m)
h	enthalpy (J/kg)
Δh	enthalpy change (J/kg)
ΔH	latent heat (J/kg)
L	total length (m)
Nu	Nusselt number (-)
M	molecular weight (kg/mol)
m	mass (kg)
$\dot{m}$	mass flow rate (kg/s)
Pr	Prandtl number (-)
Re	Reynolds number (-)
r	radius (m)
T	temperature (°C)
ΔT	temperature difference (°C)
t	time (s)
Δt	time interval (s)
u	flow velocity (m/s)
v_c	crystallization speed (mm/s)
w	mass fraction/concentration (-)
z	axial coordinate (m)
Δz	length (m)

Greeks

α	heat transfer coefficient (W/(m^2 K))
λ	thermal conductivity (W/(m K))
ρ	density (kg/m^3)
φ	volume fraction (-)

Subscripts

0	initial
amb	ambient
eq	equilibrium
f	heat transfer fluid
fin	heat transfer fluid inlet
fout	heat transfer fluid outlet
i	inner
l	liquid
p	PCM
pre	preliminary
s	solid
sup	supercooled
tp	two phase
w	wall
wat	water
wb	wall boundary

sodium acetate solution. Two different treatment methods were applied to SAT to prevent the phase separation during the phase changing, one was to add extra water and the other one was to add thickening agents. The test of SAT with 9% extra water (199.5 kg) in flat rectangular container showed the reduction of discharged thermal energy from 194 kJ/kg to 179 kJ/kg after 20 test cycles; while SAT with 1% CMC (220 kg) can maintain the discharge thermal energy at 205 kJ/kg over six test cycles. Both additions led to 45 °C discharge temperature when the heat transfer fluid flow rate at 2 L/min, and the discharge power reduced from 4.5 to 5.0 kW at the beginning to about 1.0 kW within about 4 h [8]. Similar performance was found when using a cylindrical shell-and-tube heat exchanger [9], spontaneously crystallization was noticed regardless of either addition of extra water or thickening agent when using this heat exchanger. The thermal conductivity of SAT was improved from 0.17 to 0.70 W/(m K) to 1.1 W/(m K) due to the presence of graphite powder.

The interesting discoveries in above studies encourage more efforts to explore such a promising material for seasonal solar thermal energy storage. The present paper modelled and simulated the solidification process of the supercooled SA aqueous solution to evaluate the thermal discharge performance of the storage system. Thermo-physical properties of liquid SA aqueous solution and solid SAT were both summarized, and the experimentally determined SAT crystal growth rate and the enthalpy change of the solidifying SA aqueous solution were introduced to the model in this paper for elaborating modelling.

2. Thermo-physical properties

2.1. Phase diagram

The solubility of SA in water and the melting points of SAT were experimentally measured by Green [10]. The phase diagram of sodium acetate aqueous solution is presented in Fig. 1. SAT has the salt mass fraction of 0.603 and the congruent melting point at 58.0 °C. The phase diagram was divided into six areas, including liquid SA aqueous solution area, liquid SA aqueous solution and solid SA area, liquid SA aqueous solution and solid SAT area, solid SAT and solid SA area, liquid SA aqueous solution and solid ice area, solid SAT and solid ice area. To avoid the presence of un-dissolved solid SA in the aqueous SA aqueous solution during heat charge process, the heating temperature for the pure SAT must be high enough, i.e. higher than 77.6 °C as indicated in the phase diagram. Otherwise phase separation occurs due to the larger density of solid SA. Alternatively, using leaner SA aqueous solution (< 0.58 by weight) can avoid this problem. For SAT with extra water (SA aqueous solution with concentration lower than 0.603 by weight), the phase equilibrium temperature reduces as the decrease of solution concentration, and the lowest equilibrium temperature is the eutectic melting point of ice-SAT binary system, which is −18.0 °C at the SA concentration of 0.233 by weight as shown in the phase diagram.

The measured equilibrium temperature of SA aqueous solution as the function of the solution concentration w_l were fitted by polynomial equations, Eqs. (1)–(3).

$$T_{eq} = -55.355w_l + 59.1244w_l^2 - 655.7453w_l^3 \quad 0 \le w \le 0.233 \tag{1}$$

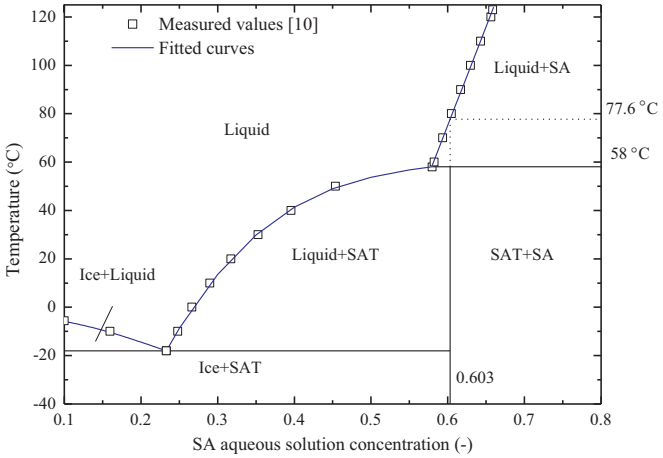

Fig. 1. Phase diagram of sodium acetate aqueous solution.

$$T_{eq} = -244.2956 + 1459.9447w_l - 2411.9539w_l^2 + 1368.4353w_l^3 \quad 0.233 < w \leq 0.58 \tag{2}$$

$$T_{eq} = -414.213 + 815.6273w_l \quad 0.58 < w \leq 0.659 \tag{3}$$

where T_{eq} is in the unit of °C. The discrepancy between the calculated and the measured values is in the range of −4.7–2.1%.

2.2. Density

The density of solid SAT has been reported as 1450 kg/m^3, while the melted SAT has the density of 1280 kg/m^3 [11]. The density of the SA aqueous solution is dependent on the its concentration and temperature, which can be calculated by the following equation given by literature [12].

$$\rho = \rho_{wat} + Ac + BcT + CcT^2 + Dc^{3/2} + Ec^{3/2}T \tag{4}$$

where T is the solution temperature in the unit of °C, c is the solution molar concentration in the unit of mol/dm^3, ρ_{wat} is the density of pure water at the same temperate, A through E are the constants, $A = 43.64$, $B = -0.0674$, $C = 0.0006482$, $D = -2.113$, $E = -0.009843$. To calculate the density based on the solution concentration in the unit of kg (salt)/kg (solution), the used concentration c in Eq. (4) should be expressed as the function w_l (kg (salt)/kg (solution)) and then the equation becomes

$$\rho = \rho_{wat} + A\frac{w_l\rho}{1000M} + B\frac{w_l\rho}{1000M}T + C\frac{w_l\rho}{1000M}T^2 + D\left(\frac{w_l\rho}{1000M}\right)^{3/2} + E\left(\frac{w_l\rho}{1000M}\right)^{3/2}T \tag{5}$$

where M is the SA molecular mass (0.082034 kg/mol). Thereby the density of SA aqueous solution at temperature T (°C) and concentration w_l (-) can be obtained by solving the above implicit equation.

The calculated densities by Eq. (5) are exemplified in Fig. 2. The density increases as the increasing solution concentration, and it descends as the ascent of temperature. Some density values of SA aqueous solution reported by others [13–15] are also plotted in Fig. 2 for comparison. It is observed from the comparison that the above calculation equation can predict the density of SA aqueous solution with acceptable accuracy.

2.3. Specific heat

Araki et al. [16] measured the specific heats of both solid SAT and SA aqueous solution with a calorimeter. The specific heat of solid SAT, c_{ps}, was correlated with the temperature [16], the following equation was given.

$$c_{ps} = 1919.989 + 4.06T \tag{6}$$

where c_{ps} is in the unit of J/(kg K) and T is in the unit of °C. The above equation has an application range of 30.0–55.0 °C, and the corresponding specific heat is from 2041.8 to 2143.3 J/(kg K), which is lower than the value of 2790 J/(kg K) reported by literature [11].

Only the specific heats of SA aqueous solutions with the concentration of 0.603 and 0.543 were measured within the temperature range of 30.0–80.0 °C by Araki et al. [16]. Based on these measured values and the theoretical specific heat of pure water [13], the calculation equation of c_p of the SA aqueous solution at different concentration and different temperature has been developed by the present study as expressed in Eq. (7).

$$c_{pl} = c_{pwat} + w_l(A + BT + CT^2) \tag{7}$$

where c_{pwat} is the specific heat of pure water at the same temperature, A through C are the fitted constants, $A = -2424.316$, $B = 8.38833$, $C = -0.01456$. The equation is applicable for the temperature range of 30.0–80.0 °C and the concentration range of 0–0.603. As shown in Fig. 3, the discrepancy between the calculated and the experimentally measured values are within ± 0.6%.

Another two groups of measured c_p of SA aqueous solution were used to compare and validate the developed equation of Eq. (7). The measured c_p of the melted SAT ($w_l = 0.603$) reported by Li et al. [15] is only about 1.5–1.8% lower than the calculated results by Eq. (7). The other group of measured c_p of SA aqueous solution with 0.04–0.372 concentration at 25 °C reported by Bochmann et al. [17] are also plotted in the figure, only the c_p value of the solution with 0.372 concentration has apparent deviation from the calculated result by Eq. (7).

With the known specific heats of solid SAT and liquid SA aqueous solution, the overall specific heat of the two-phase mixture can be calculated by Eq. (8).

$$c_{ptp} = wc_{ps} + c_{pl}(1-w) \tag{8}$$

where w is the mass fraction of the solid phase in the mixture.

2.4. Thermal conductivity

Araki et al. [16] also measured the thermal conductivities of solid SAT and SA aqueous solution by using thermistor chip and electric circuit. The thermal conductivity of the solid SAT can be treated as a constant at 0.7 W/(m K) within the temperature range of 20.0–40.0 °C. The thermal conductivity of SA aqueous solution with the concentration of 0.453–0.603 at 20.0–70.0 °C were measured, which decreased with increasing temperature and solution concentration. It should be mentioned that the thermal conductivity of pure water generally increases as the temperature rising.

The experimental results reported by Araki et al. [16] were fitted by the following equation (Eq. (9)) by the present study.

$$\lambda_l = (A + BT + CT^2)(D + Ew_l + Fw_l^2 + Gw_l^3) \tag{9}$$

where the values of the constants A through G are 0.42046, 0.00152, −0.0000358996, −3.11723, 25.6774, −51.24218 and 33.1474 respectively. The fitting error is in the range of −3.4–2.3%, as presented in Fig. 4. Then the thermal conductivity of the two-phase mixture, i.e. solid SAT and liquid SA aqueous solution, can be estimated by the well-known Maxwell-Eucken equation [18] as expressed in Eq. (10).

$$\lambda_{tp} = \lambda_l\frac{2\lambda_l + \lambda_s - 2\varphi(\lambda_l - \lambda_s)}{2\lambda_l + \lambda_s + \varphi(\lambda_l - \lambda_s)} \tag{10}$$

where φ is the volume fraction of the solid in this mixture. If the solid volume fraction is larger than 0.5, λ_l and λ_s should swap the position as the solid becomes continuous phase and the liquid becomes dispersed phase, and φ should be the volume fraction of the liquid.

The thermal conductivities of the melted SAT measured by Li et al.

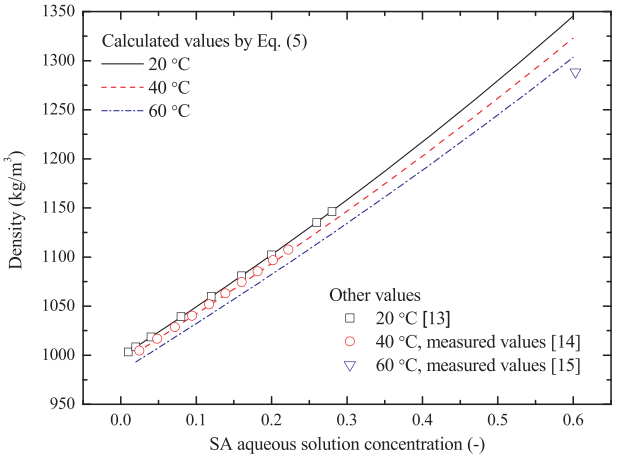

Fig. 2. Calculated densities of SA aqueous solution and the comparison with other reported values.

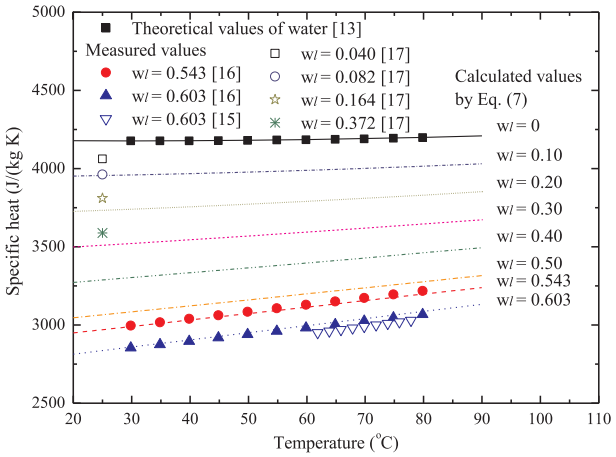

Fig. 3. Calculated and measured specific heats of SA aqueous solution at different temperature and concentration.

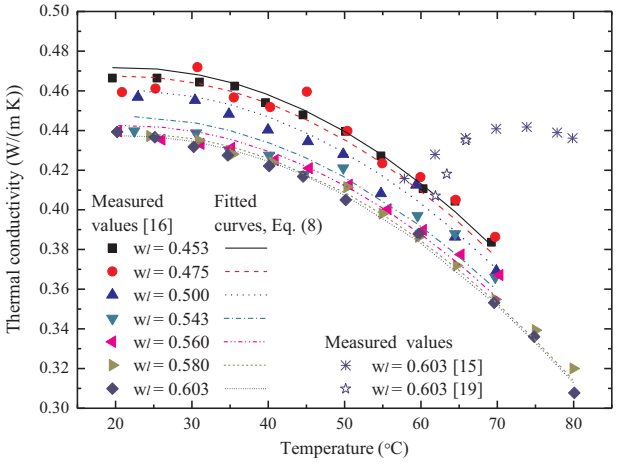

Fig. 4. Thermal conductivities of SA aqueous solution at different temperature and concentrations.

[15] and Peng et al. [19] have closed values as shown in Fig. 4; however, these values represent the thermal conductivity of liquid SA aqueous solution prepared by melting the solid SAT, and they deviated from Araki et al.'s result which was measured directly on the aqueous solution [16], as can be seen from Fig. 4.

3. Mathematic model

The solidification process of the supercooled SA aqueous solution in a single cylindrical storage tube was modelled in the present study, which can be treated as a fundamental model of a typical shell-tube heat exchanger with PCM filled inside the tube and the heat transfer fluid (HTF) flowing outside the tube.

To avoid high heating temperature (> 77.6 °C) required by the melting of pure SAT during heat charge stage, SA aqueous solution with 0.58 concentration was used as the initial solution, of which the melting temperature was 58.0 °C. In this instance, the presence of un-dissolved solid SA particle could be avoided during the heat charge stage.

The following assumptions have been made for the modelling.

- The tube has large length-to-radius ratio, therefore the heat transfer inside the PCM is only along the axial direction;
- The solidification of the supercooled SA aqueous solution is initiated at the top of the tube, hence the SAT crystal grows from the top to the bottom;
- The heat convection of the liquid solution is negligible since its temperature would be higher at the top and lower at the bottom during the solidification process.
- The whole storage system is at ambient temperature before the solidification due to the seasonal storage, while the inlet of the HTF is at ambient temperature as well.

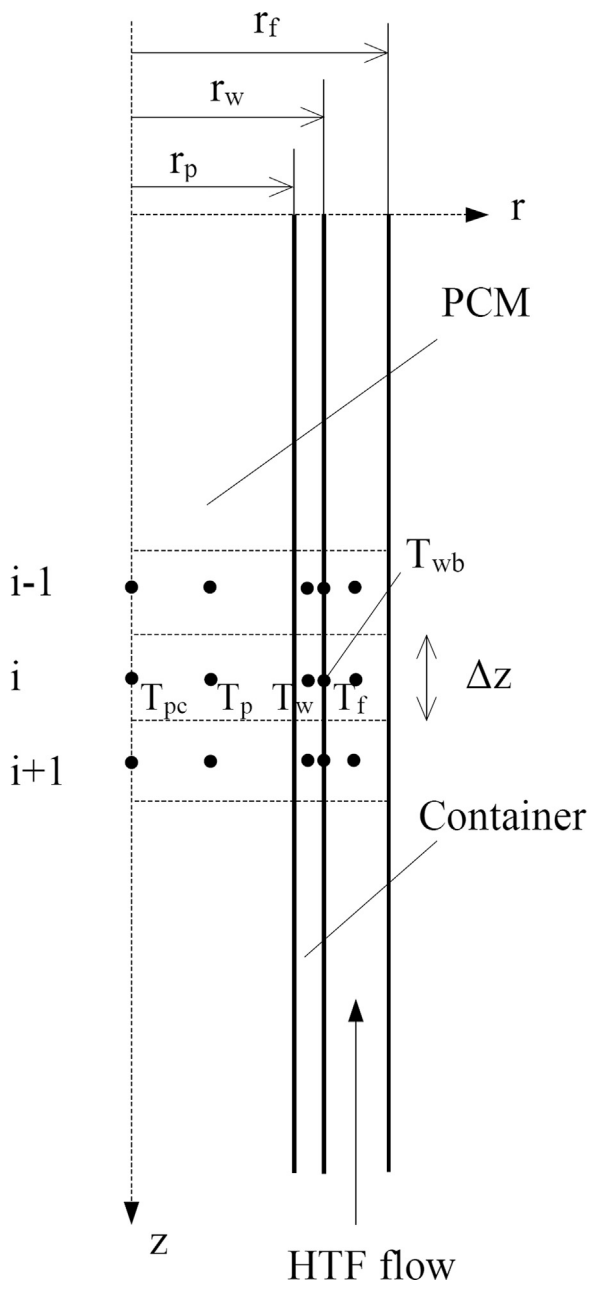

Fig. 5. Physical model of the solidification process of supercooled SA aqueous solution in a single tube container.

3.1. Heat transfer equations

The schematic diagram of the heat transfer is shown in Fig. 5. The tube has the total length of L, the inner radius of r_p and outer radius r_w, while the outer boundary of the HTF has the radius of r_f. The PCM, the tube wall and the HTF are all divided into small control volume along the axial direction with the same interval, Δz.

The heat conduction equation of the solidifying SA aqueous solution is based on the enthalpy change of the solution, as given in Eq. (11), while the heat conduction equation and heat convection equation of tube wall and HTF are given as Eqs. (12) and (13) respectively.

$$\rho\frac{\partial h_p}{\partial t} = \frac{1}{r}\frac{\partial}{\partial r}\left(r\lambda\frac{\partial T_p}{\partial r}\right) + \frac{\partial}{\partial z}\left(\lambda\frac{\partial T_p}{\partial z}\right) \tag{11}$$

$$\rho c_p\frac{\partial T_w}{\partial t} = \frac{1}{r}\frac{\partial}{\partial r}\left(r\lambda\frac{\partial T_w}{\partial r}\right) + \frac{\partial}{\partial z}\left(\lambda\frac{\partial T_w}{\partial z}\right) \tag{12}$$

$$\rho c_p\frac{\partial T_f}{\partial t} + \rho c_p u\frac{\partial T_f}{\partial z} = \frac{1}{r}\frac{\partial}{\partial r}\left(r\lambda\frac{\partial T_f}{\partial r}\right) + \frac{\partial}{\partial z}\left(\lambda\frac{\partial T_f}{\partial z}\right) \tag{13}$$

The initial condition of all control volumes is given as Eq. (14).

$$T_{t=0} = T_{amb} \tag{14}$$

For the SA aqueous solution, the symmetry leads to the following boundary condition at $r = 0$.

$$\left.\frac{\partial T_p}{\partial r}\right|_{r=0} = 0 \tag{15}$$

For the tube wall, the boundary condition on the HTF side is formulated as Eq. (16).

$$-\lambda\left.\frac{\partial T_w}{\partial r}\right|_{r=r_w} = \alpha(T_f - T_{wb}) \tag{16}$$

where T_{wb} is the temperature of tube wall surface as shown in Fig. 5, α is the heat transfer coefficient of the flowing HTF, which can be calculated by Dittus and Boelte's equation [20], Eq. (17), for turbulent flow.

$$Nu = \frac{\alpha D_e}{\lambda} = 0.023Re^{0.8}Pr^{0.4} \tag{17}$$

For a fully developed laminar flow in an annular channel, the Nusselt number can be treated as constant; Eq. (18) was developed by the present study based on the Nusselt numbers given in literature [20] for annular channel with D_i/D_o in the range of 0.5–1.0.

$$Nu_i = \frac{\alpha D_i}{\lambda} = 5.74 - 1.76\left(\frac{D_i}{D_o} - 0.5\right) \tag{18}$$

where Nu_i is the inner surface Nusselt number and D_i is the inner diameter of the annual channel.

The inlet of the HTF flow is retained at a constant temperature as Eq. (19).

$$T_{f\,z=L} = T_{fin} \tag{19}$$

The above heat transfer equations were explicitly solved due to the involved PCM enthalpy, h_p, in Eq. (11), then the time step was sufficiently low to ensure the convergent calculation.

3.2. Enthalpy change of solidifying SA aqueous solution

The enthalpy change Δh of the phase changing PCM with a temperature difference ΔT and a solid mass fraction change Δw can be obtained through the calculation of Eq. (20).

$$\Delta h = \Delta T c_{pl}(1 - w) + \Delta T c_{ps} w + \Delta H \Delta w \tag{20}$$

where w is the solid mass fraction after phase change, c_{ps} and c_{pl} are the mean specific heats of the solid and liquid PCM respectively within the temperature range, ΔH is the latent heat of the phase change. Assuming the enthalpy $h = 0$ at $T = 80$ °C, the equilibrium enthalpy of the solidifying SA aqueous solution with 0.58 concentration is shown in Fig. 6. The figure also shows the enthalpy variation of the aqueous solution when its temperature drops to supercooling level, which can be obtained based on its specific heat.

The solidification of the supercooled SA aqueous solution starts from point A ($T_{amb} = 10$ °C as an example) in Fig. 6; the exothermic phase change results in temperature increase until the solution reaches point B at the equilibrium enthalpy curve; since then the state of the formed solid-liquid two-phase mixture follows the equilibrium enthalpy curve till the temperature drops to the ambient temperature at point C. The trajectory from point A to B is dominated by the heat transfer and crystal growth rate. Between points A and B, the mass fraction of the formed solid SAT crystal at a certain temperature T with a given enthalpy h can be calculated by the following equation as suggested and validated by Gunther et al. [21].

$$w = \frac{T - T_{sup}}{T_{eq} - T_{sup}} w_{eq} \tag{21}$$

where T_{sup} is the temperature of supercooled solution with an enthalpy value of h, T_{eq} and w_{eq} are the equilibrium temperature and mass fraction of the solidifying SA aqueous solution with the enthalpy h, respectively. The mass fraction on the equilibrium enthalpy curve, w_{eq} can be calculated by the following equation based on mass balance.

$$w_{eq} = \frac{w_0 - w_l}{w_{hyd} - w_l} \tag{22}$$

where w_0 is the initial solution concentration, w_l is the saturated solution concentration at the temperature T, w_{hyd} is the mass fraction of salt in the hydrate crystal (0.603 for SAT).

3.3. Crystal growth rate

Munakata and Nagata [22] and Dietz et al. [23] have measured the crystal growth rate, v_c, of supercooled SA aqueous solution in tubes. The growth rates were found to be independent on the tube size and the time after the crystallization being initiated, but only the function of solution concentration and supercooling degree [22,23]. These two measurements obtained close values and similar variation pattern as shown in Fig. 7.

The crystal growth rate was correlated with initial solution concentration, w_0, and supercooling degree, ΔT_{sup}, as Eq. (23), by Munakata and Nagata [22].

$$v_c = (18.6w_0 - 6.93)\left[1 + Erf\left(\frac{\Delta T_{sup} + 60.0w_0 - 45}{7.5}\right)\right] \tag{23}$$

where v_c is in the unit of mm/s. The application scope of the above equation is limited to $w_0 = 0.40$–0.55 and $\Delta T_{sup} = 0$–48 °C. The comparison between the calculated results and the measured results of two works [22,23] is shown in Fig. 7, where it is observable that the equation provides better prediction on the cases with high solution concentration and large supercooling degree than that with low solution concentration and small supercooling degree.

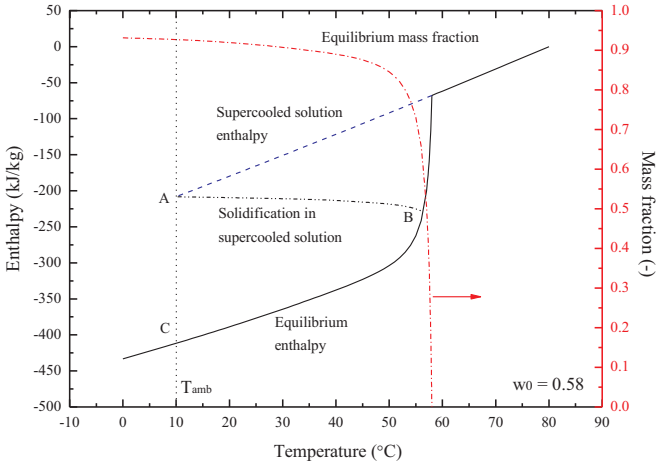

Fig. 6. Enthalpy and mass fraction of the solidifying SA aqueous solution with 0.58 concentration.

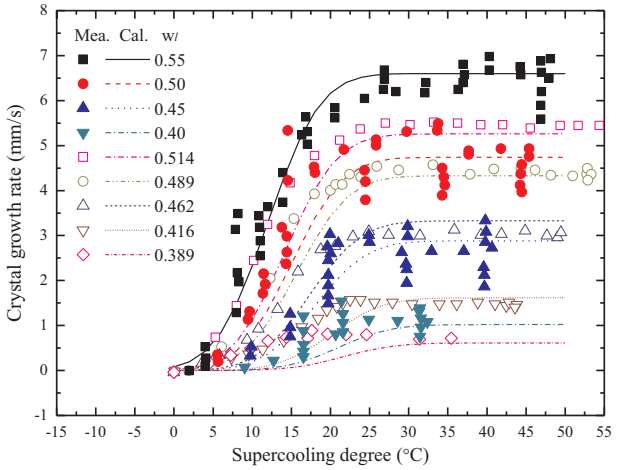

Fig. 7. Measured and calculated crystal growth rates of SAT; solid symbols are the measured values from literature [22], open symbols are the measured values from literature [23], the calculated values are calculated by Eq. (23).

3.4. Simulation process

The enthalpy and mass fraction changes discussed in Section 3.2 and the measured crystal growth rate in Section 3.3 were introduced to assist the simulation, the following steps were employed.

(1) Input all the initial parameters, including the dimensions of the tube and the HTF flow channel, the initial solution concentration, the ambient temperature and the HTF mass flow rate. These values used in the present work are given in Table 1. The tube is made of stainless steel. The thermal properties of the tube and the HTF (water) can be referred to the literature [13].
(2) The average liquid temperature at the previous time step is used to calculate the supercooling degree, then the crystal growth rate can be obtained through Eq. (23). The crystal growth rate is used to determine the interface between the phase changed and unchanged. A preliminary value of the solid mass fraction, w_{pre}, of each control volume is obtained depending on the position of the interface, w_{pre} = 0–1.0 for the control volume contains the interface, w_{pre} = 1.0 for those control volumes above the interface, w_{pre} = 0 for those control volumes below the interface. However, the solid mass fraction can never reach 1.0 as illustrated in Fig. 6 because of the incongruent solidification, the material above the interface is actually in solid-liquid two-phase rather than in pure solid state, and the solidification continues if the temperature keeps declining. Therefore this preliminary mass fraction value must be corrected in the next step.
(3) The enthalpies of all the PCM control volumes at the present time step are explicitly calculated by Eq. (11) using the temperature at the previous time step, and these enthalpies are used to determine the equilibrium solid mass fraction. If w_{pre} obtained in Step (2) is smaller than this equilibrium mass fraction, w_{pre} is considered as the real mass fraction and the present temperature is calculated by Eq. (21); otherwise, the present temperature is considered as the equilibrium temperature at the present enthalpy and the real mass fraction is re-calculated by Eq. (22).
(4) Temperatures of the tube and the HTF are explicitly calculated by Eqs. (12) and (13) using the temperatures at the previous time step.
(5) Step (2) to (4) are repeated with the given time interval Δt till reaching the pre-defined discharge time.

4. Modelling results and discussion

The temperature variation during the thermal discharge of the storage system is exemplified in Fig. 8(a) in the case of 10 °C ambient temperature and 0.001 kg/s mass flow rate of HTF. The PCM temperature, tube temperature and HTF temperature at $z = L/2$, and the HTF outlet temperature at $z = 0$ are presented. At the very beginning of the solidification, as the SA aqueous solution is at deep supercooling state, the crystal growth rate reaches its maximum value, therefore the PCM temperature surges drastically to its equilibrium temperature (corresponding to the process A to B shown in Fig. 6) because of the violent exothermic phase change. The solidification process is subsequently slowing down and the enthalpy of the solidifying SA aqueous solution traces the curve of equilibrium enthalpy shown in Fig. 6 (process B to C). In this stage, the exothermic phase change releases heat to the lower temperature HTF to get further solidification, and the crystal growth rate of SAT is mainly limited by the heat transfer conditions in the storage system. The temperature of tube wall and HTF inside storage system (between shell and tube) rises to about 36.5 °C and 26.0 °C respectively within 30 min under the current study conditions, and then both temperature are nearly constant for almost 2 h. More importantly, the outlet temperature of HTF (at $z = 0$) reaches its plateau at about 35.2 °C after 45 min heating up and lasts for around 2 h. This temperature can sufficiently meet the demand of the space heating.

The overall released/consumed thermal powers of different components in the storage system during the solidification process are shown in Fig. 8(b). The released thermal power by the solidifying SA aqueous solution surges up to about 187.1 W within the first 3 min, then it decreases to about 105.5 W after 45 min, thereafter this thermal power reaches a short plateau and then decreased gently. Only sensible heats are consumed by the tube container and the HTF inside the system, their corresponding thermal powers increase sharply following that of PCM, then decrease down to around zero after their temperatures reach the plateau. The output thermal power by flowing HTF has the same variation profile as the HTF outlet temperature, which reaches its maximum value of 105.3 W within 45 min and remains at this level about 2 h before it gradually drops down. It is noticeable that the declining output thermal power of the HTF is slightly larger than the power released by the solidifying PCM. This can be explained by the heat transfer from the tube and HTF inside the storage system to the flowing HTF, and can be evidenced by the negative values of the thermal power of these two components started at Hour 2.

During the seasonal storage, the PCM, the container and the HTF inside the storage system gradually lose their sensible heat to the ambient, so that the entire system is at the ambient temperature at the beginning of the thermal discharge stage. Meanwhile the inlet HTF temperature is assumed to be constant at ambient temperature. The corresponding variations of the outlet HTF temperature and output thermal power as the ambient temperature decreasing from 15 °C to 0 °C are shown in Fig. 9(a) and (b), respectively. The maximum temperature of the outlet HTF achieves at about 45 min after the solidification launches, and it is 30.4 °C, 32.8 °C, 35.2 °C, and 37.5 °C respectively when the ambient temperature is at 0 °C, 5 °C, 10 °C and 15 °C; accordingly, the temperature lift decreases from 30.4 °C to 22.5 °C as

Table 1
Parameters used in the present calculation.

Parameter	Unit	Value
L	mm	1000
r_p	mm	50
r_w	mm	51
r_f	mm	56
Δz	mm	20
m_p	kg	10.51–10.65
w_0	–	0.58
T_{amb}	°C	0.0–15.0
$\dot{m}_f$	kg/s	0.001–0.008
Δt	s	0.2

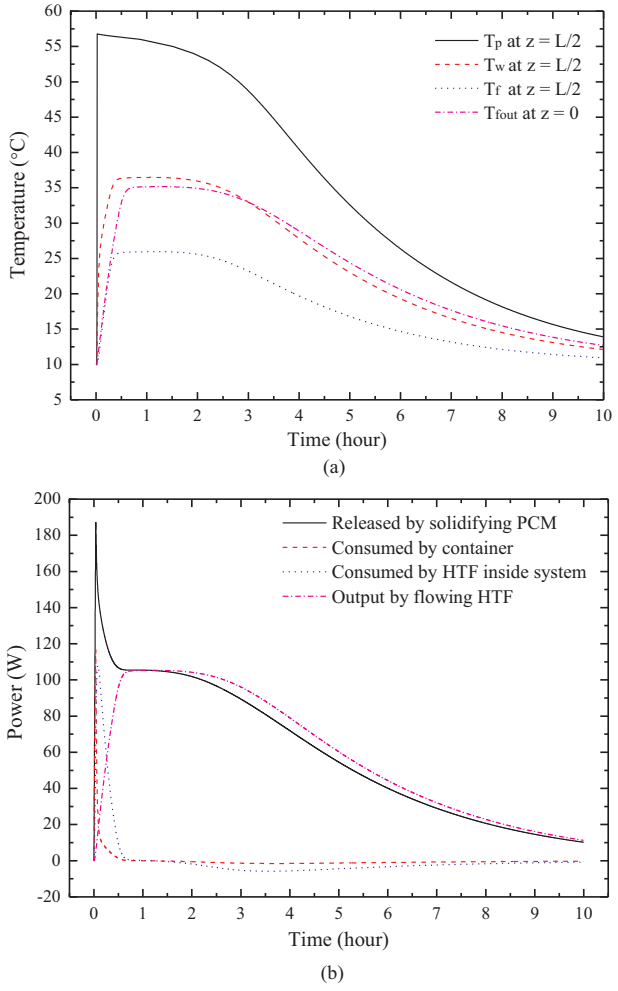

Fig. 8. Variations of (a) temperature and (b) thermal power during the solidification of SA aqueous solution, T_{amb} = 10 °C, $\dot{m}_f$ = 0.001 kg/s.

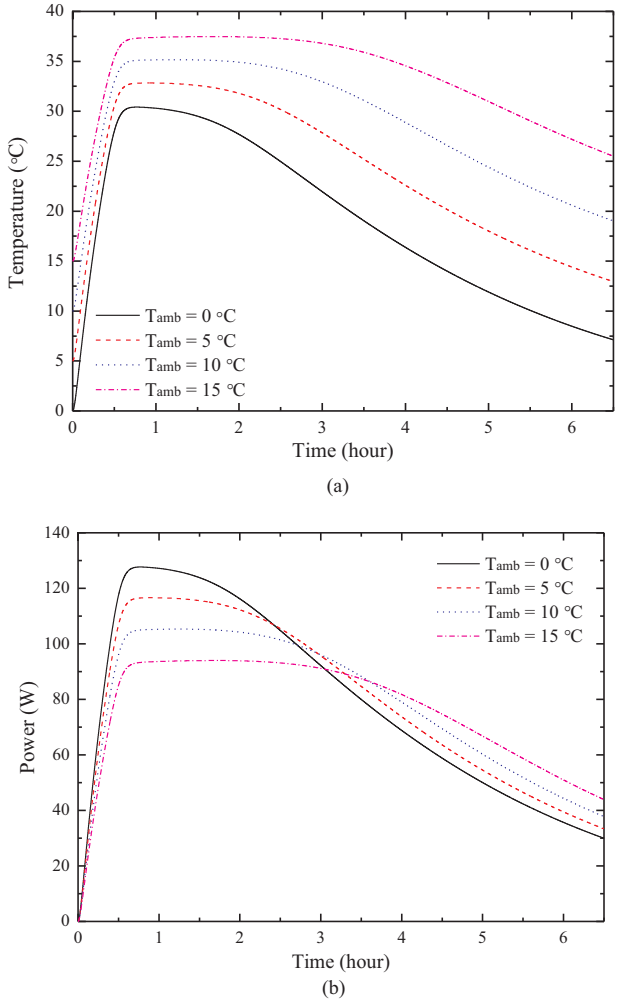

Fig. 9. Influence of the ambient temperature on (a) HTF outlet temperature; (b) output thermal power, $\dot{m}_f$ = 0.001 kg/s.

the ambient temperature increases from 0 °C to 15 °C; however, the duration of the HTF outlet temperature retaining at the maximum level is longer when the ambient temperature is higher. The lower ambient temperature leads to larger supercooling degree of the stored SA aqueous solution and larger temperature difference between the solidifying PCM and HTF, resulting in higher discharge thermal power, as shown in Fig. 9(b). That also explains the larger HTF temperature lift with lower ambient temperature and steeper changes of the HTF temperature and releasing power, while there is more gentle and smooth variation with higher ambient temperature, leading to the longer duration of the plateau of the curves with higher ambient temperature.

Fig. 10 shows the influence of the HTF mass flow rate on the heat discharge performance, taking T_{amb} = 10 °C as an example. Apparently, higher mass flow rate of the HTF leads to lower temperature lift, as shown in Fig. 10(a), the maximum HTF outlet temperature decreases from about 35.2 °C to 14.3 °C as the mass flow rate increasing from 0.001 kg/s to 0.008 kg/s. Nevertheless, for the first 3 h in Fig. 10(b), the HTF at higher mass flow rate delivers higher thermal power, e.g. the maximum output power increases from 105.3W to 144.9 W as the mass flow rate increasing from 0.001 kg/s to 0.008 kg/s. This is because of the larger temperature difference between the exothermic PCM and the flowing HTF when the HTF is at higher mass flow rate. After these first 3 h, it becomes opposite that the HTF at lower mass flow rate delivers slightly higher thermal power. That suggests that the setting value of the HTF mass flow rate should be deliberated over the balance between satisfactory HTF outlet temperature and output thermal power.

To pursue higher HTF outlet temperature to meet the need of space heating, the HTF mass flow rate should be relatively low, as the foregoing discussion, which implies that the heat convection of HTF can be inevitably unsatisfactory. For example, the present calculation shows that the HTF flow is in the region of laminar flow when the mass flow rate is in the range of 0.001–0.008 kg/s, and the heat transfer coefficient is only 29–32 W/(m^2 K). This poses an obstacle for the practical application of this storage system. The heat transfer coefficient can be promoted by enforcing the flow turbulence of the HTF. Fig. 11 is plotted with the enhanced performance when the heat transfer coefficient is improved from 30 W/(m^2 K) to 200 W/(m^2 K), in the case of 10 °C ambient temperature and 0.001 kg/s HTF mass flow rate. Both the HTF outlet temperature and output power are prominently improved by using larger heat transfer coefficient, e.g. the maximum HTF outlet temperature is elevated from 35.2 °C to 41.1 °C and the corresponding output thermal power is increased from 105.3W to 130.2 W when the heat transfer coefficient is from 30 W/(m^2 K) to 200 W/(m^2 K). However, the plateau of both the temperature and power were shorter considering the energy balance between the exothermic PCM and HTF.

5. Energy density

The energy density of SAT (w_0 = 0.58) was obtained based on current modelling results when considering 20 °C as the lower limit of HTF outlet temperature during the thermal discharge. Fig. 12 shows both of the pure material energy density and system energy density in the unit of kW h/m^3, and also the comparison with those of the sensible

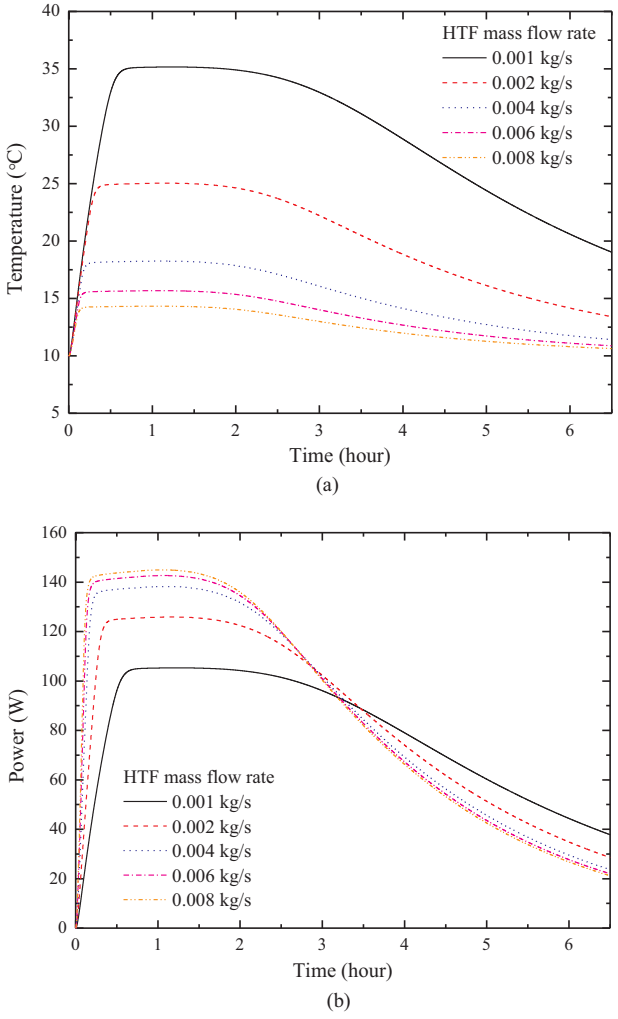

Fig. 10. Influence of the mass flow rate of HTF on (a) HTF outlet temperature; (b) output thermal power, T_{amb} = 10 °C.

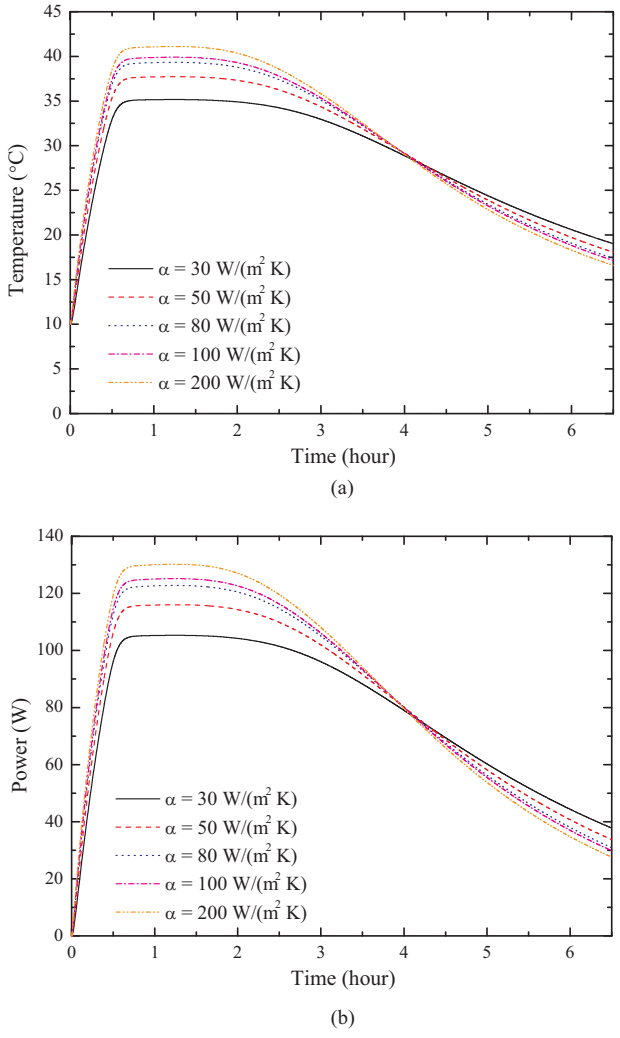

Fig. 11. Influence of heat transfer coefficient on (a) HTF outlet temperature; (b) output thermal power by HTF, T_{amb} = 10 °C, $\dot{m}_f$ = 0.001 kg/s.

heat storage using water and sorption heat storage using LiCl-water, zeolite-water and silica gel-water experimentally tested and reported by literature [24]. To get fair comparison, the discharge start temperature was considered as the horizontal axis, which reflected the thermal insulation condition of the storage system. Apparently, better insulation leads to higher discharge start temperature and larger energy density as shown in the figure. At the same discharge start temperature, the material energy density of SAT is substantially higher than that of water; and even without thermal insulation, i.e. the discharge start temperature is at atmosphere temperature of winter, the material energy density of SAT is at the same level as that of water with 70–80 °C discharge start temperature. This is a huge advantage of using SAT for seasonal thermal energy storage. The material energy density of SAT is apparently less than that of sorption storage materials LiCl-water and zeolite-water reported in literature [24]; nevertheless, the sorption storage system has much complicated configuration than that of SAT, since there is additional condenser/evaporator in the sorption system and the sorption material must have mass transfer channels for the vapour which make the sorption system bulky, therefore the system energy density of SAT can be competitive to those of sorption systems as shown in the figure.

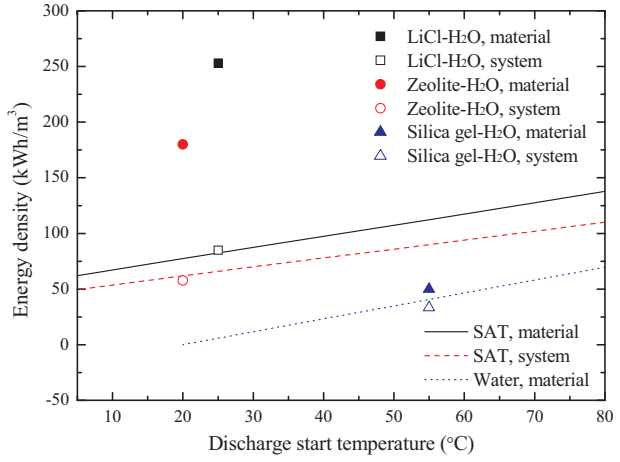

Fig. 12. Material and system energy densities of SAT (w_0 = 0.58) and other technologies for seasonal thermal storage, the results of sorption materials are from literature [24].

6. Conclusions

Sodium acetate trihydrate was studied in the present paper as a seasonal solar thermal energy storage material. The calculation methods of the thermo-physical properties, including the equilibrium temperature, densities, specific heats and thermal conductivities of the solid SAT, liquid SA aqueous solution and the two-phase mixture have been built. The thermal discharge process of the storage system, i.e. the solidification process of the supercooled SA aqueous solution, was modelled with the aid of enthalpy change curve and crystal growth rate.

The primary findings are made as follows.

(a) The solidification process was violent at the very beginning since the aqueous solution was at the deep supercooling state, thereafter the solidification was slow down and the enthalpy followed the equilibrium enthalpy curve which was dominated by the heat transfer condition.
(b) For a single tube storage system with 10.51–10.65 kg PCM, the HTF outlet temperature could reached 30.4–37.5 °C when the ambient temperature was in the range of 0–15 °C and the mass flow rate of HTF was 0.001 kg/s. This indicate the quality of discharged heat was enough to do space heating. The corresponding output thermal power was in the range of 94.0–127.7 W, which can be improved by adding more storage units into the system.
(c) By increasing the mass flow rate of HTF to achieve higher output thermal power was not a good choice in current storage system, since the HTF outlet temperature would reduce accordingly, which was then not high enough for space heating. One should balance the choice between the increasing output thermal power and the reducing HTF outlet temperature.
(d) To gain the qualified HTF for space heating, the used mass flow rate of HTF should be relatively low which caused the poor heat transfer between the solidifying PCM and the flowing HTF. This can be promoted by enhancing the flow turbulence of HTF. As the heat transfer coefficient was improved from 30 W/(m^2 K) to 200 W/(m^2 K), the maximum HTF outlet temperature could be promoted from 35.2 °C to 41.1 °C and the corresponding output thermal power was from 105.3W to 130.2 W in the case of 10 °C ambient temperature and 0.001 kg/s HTF mass flow rate.
(e) The material energy density of SAT without thermal insulation was still at the same level of that of water with 70–80 °C discharge start temperature; the system energy density of SAT could be competitive to that of sorption system due to its much simpler system configuration.

Acknowledgement

The authors gratefully acknowledge the support from the Heat-STRESS project (EP/N02155X/1) funded by the Engineering and Physical Science Research Council. Data supporting this publication is openly available under an 'Open Data Commons Open Database License'. Additional metadata are available at: http://dx.doi.org/10.17634/152536-3.

References

[1] P. Pinel, C.A. Cruickshank, I. Beausoleil-Morrison, A. Wills, A review of available methods for seasonal storage of solar thermal energy in residential applications, Renew. Sustain. Energy Rev. 15 (2011) 3341–3359.
[2] J. Xu, R.Z. Wang, Y. Li, A review of available technologies for seasonal thermal energy storage, Sol. Energy 103 (2014) 610–638.
[3] K.E. N'Tsoukpoe, H. Liu, N.L. Pierres, L. Luo, A review on long-term sorption solar energy storage, Renew. Sustain. Energy Rev. 13 (2009) 2385–2396.
[4] B. Zalba, J.M. Marin, L.F. Cabeza, H. Mehling, Review on thermal energy storage with phase change: materials, heat transfer analysis and applications, Appl. Therm. Eng. 23 (2003) 251–283.
[5] L. Wei, K. Ohsasa, Supercooling and solidification behaviour of phase change material, ISIJ Int. 50 (2010) 1265–1269.
[6] M. Dannemand, J.M. Schultz, J.B. Johansen, S. Furbo, Long term thermal energy storage with stable supercooled sodium acetate trihydrate, Appl. Therm. Eng. 91 (2015) 671–678.
[7] M. Dannemand, J.B. Johansen, S. Furbo, Solidification behaviour and thermal conductivity of bulk sodium acetate trihydrate composites with thickening agents and graphite, Sol. Energy Mater. Sol. Cells 145 (2016) 287–295.
[8] M. Dannemand, J. Dragsted, J. Fan, K.B. Johansen, W. Kong, S. Furbo, Experimental investigation on prototype heat storage units utilizing stable supercooling of sodium acetate trihydrate mixtures, Appl. Energy 169 (2016) 72–80.
[9] M. Dannemand, J.B. Johansen, W. Kong, S. Furbo, Experimental investigation on cylindrical latent heat storage units with sodium acetate trihydrate composites utilizing supercooling, Appl. Energy 177 (2016) 591–601.
[10] W.F. Green, The 'melting-point' of hydrated sodium acetate: solubility curves, J. Phys. Chem. 12 (1908) 655–660.
[11] G. Bajnoczy, E.G. Palffy, E. Prepostffy, A. Zold, Thermal properties of a heat storage device containing sodium acetate trihydrate, Period. Polytech. Chem. Eng. 39 (1995) 129–135.
[12] P. Novotny, O. Sohnel, Densities of binary aqueous solutions of 306 inorganic substances, J. Chem. Eng. Data 33 (1988) 49–55.
[13] R.H. Perry, D.W. Green, J. O'Hara Maloney, Perry's Chemical Engineers' Handbook, 7th edition, Mcgraw-Hill, United States, 1997.
[14] G.M. Watson, W.A. Felsing, The apparent and partial molal volumes of the sodium salts of formic, acetic, propionic and n-butyric acids in aqueous solution, J. Am. Chem. Soc. 63 (1941) 410–412.
[15] Y. Li, T. Inagaki, H. Kashiwa, Thermo-physical properties of phase change materials and those natural convection heat transfer in a horizontal enclosed rectangular container, Appl. Mech. Mater. 620 (2014) 468–471.
[16] N. Araki, M. Futamura, A. Makino, H. Shibata, Measurements of thermophysical properties of sodium acetate hydrate, Int. J. Thermophys. 16 (1995) 1455–1466.
[17] S. Bochmann, P.M. May, G. Hefter, Molar volumes and heat capacities of aqueous solutions of short-chain aliphatic sodium carboxylates at 25 °C, J. Chem. Eng. Data 56 (2011) 5081–5087.
[18] A. Eucken, Allgemeine Gesetzmäßigkeiten für das Wärmeleitvermögen verschiedener Stoffarten und Aggregatzustände, Forsch. Geb. Ing. A 11 (1940) 6–20.
[19] W. Peng, J.M. Zhou, Y. Li, Y. Yang, M.R. Guo, A dynamic technique for the measurement of thermal conductivity of molten salt based on cylindrical melting model, J. Therm. Anal. Calorim. 115 (2014) 1767–1777.
[20] W.M. Rohsenow, J.P. Hartnett, Handbook of Heat Transfer, McGraw-Hill, USA, 1973.
[21] E. Gunther, H. Mehling, S. Hiebler, Modeling of subcooling and solidification of phase change materials, Model. Simul. Mater. Sci. Eng. 15 (2007) 879–892.
[22] T. Munakata, S. Nagata, Study on solidification process of sodium acetate trihydrate from supercooled state, Trans. Jpn. Soc. Mech. Eng. (B) 74 (2008) 2365–2371.
[23] P.L. Dietz, J.S. Brukner, C.A. Hollingsworth, Linear crystallization velocities of sodium acetate in supersaturated solutions, J. Phys. Chem. 61 (1957) 944–948.
[24] C. Bales, Laboratory tests of chemical reactions and prototype sorption storage units, IEA SHC Task 32 Subtask B 'Chemical and Sorption Storage'. ⟨http://task32.iea-shc.org/data/sites/1/publications/task32-b4.pdf⟩ (Accessed 11 January 2017).